Scattering-dependent transport of $SrRuO_3$ films: From Weyl fermion transport to hump-like Hall effect anomaly

Shingo Kaneta-Takada,[1,2,*] Yuki K. Wakabayashi,[1,*,†] Yoshiharu Krockenberger,[1] Hiroshi Irie,[1] Shinobu Ohya,[2,3] Masaaki Tanaka,[2,3] Yoshitaka Taniyasu,[1] and Hideki Yamamoto[1]

[1]*NTT Basic Research Laboratories, NTT Corporation, Atsugi, Kanagawa 243-0198, Japan*

[2]*Department of Electrical Engineering and Information Systems, The University of Tokyo, Bunkyo, Tokyo 113-8656, Japan*

[3]*Center for Spintronics Research Network (CSRN), The University of Tokyo, Bunkyo, Tokyo 113-8656, Japan*

(Received 9 February 2023; accepted 2 May 2023; published 30 May 2023)

Recent observation of quantum transport phenomena of Weyl fermions has brought much attention to 4*d* ferromagnetic perovskite $SrRuO_3$ as a magnetic Weyl semimetal. Additionally, the hump-like Hall effect anomaly, which might have a topological origin, has been reported for this material. Here, we show that the emergence of such phenomena is governed by the degree of scattering determined by the defect density (Ru-deficiency- and/or interface-driven-defect scattering) and measurement temperature (phonon scattering), where the former is controlled by varying the growth conditions of the $SrRuO_3$ films in molecular beam epitaxy as well as the film thickness. The resulting electronic transport properties can be classified into three categories: clean, intermediate, and dirty regimes. The transport of Weyl fermions emerges in the clean regime, whereas that of topologically trivial conduction electrons in the ferromagnetic metal state prevails in the intermediate and dirty regimes. In the clean and intermediate regimes, anomalous Hall resistivity obeys a scaling law incorporating the intrinsic Karplus-Luttinger and extrinsic side-jump mechanisms. The hump-like Hall effect anomaly is observed only in the dirty regime, which is contrary to the scaling law between anomalous Hall resistivity and longitudinal resistivity. Hence, we conclude that this anomaly is not inherent to the material and does not have a topological origin. We also provide defect- and temperature-dependent transport phase diagrams of stoichiometric $SrRuO_3$ and Ru-deficient $SrRu_{0.7}O_3$ where the appearance of Weyl fermions and hump-like Hall effect anomaly is mapped. These diagrams may serve as a guideline for designing $SrRu_{1-x}O_3$-based spintronic and topological electronic devices.

DOI: 10.1103/PhysRevMaterials.7.054406

I. INTRODUCTION

Topological materials have attracted much attention for future applications in spintronics and topological electronics [1]. Functional devices such as racetrack memory [2,3] utilizing skyrmions [4] and topoelectrical circuits [5,6] utilizing Weyl fermions have been proposed [7,8]. Weyl fermions emerge at the spin-split band crossing points in momentum space with spin-orbit interaction [9–12]. They show transport phenomena related to pairs of Weyl nodes, such as chiral-anomaly-induced negative magnetoresistance (MR), unsaturated linear positive MR, the π Berry phase along cyclotron orbits, light cyclotron masses, and high quantum mobility [13]. Meanwhile, skyrmions are topologically nontrivial spin textures derived from a correlation between a strong Dzyaloshinskii-Moriya interaction and a ferromagnetic exchange interaction. A skyrmion creates the Berry curvature and provides additional transverse electron scattering, leading to the hump-like Hall effect anomaly, the so-called topological Hall effect [14].

In recent years, itinerant 4*d* ferromagnetic perovskite $SrRuO_3$ has attracted intense interest due to the emergence of Weyl fermions in oxides [15,16] and the hump-like Hall effect anomaly that possibly arises from the topologically nontrivial spin texture [17–19]. The existence of Weyl fermions is well established, and high-quality $SrRuO_3$ films show quantum transport of bulk three-dimensional Weyl fermions and two-dimensional Weyl fermions from surface Fermi arcs [20,21]; in our previous studies [16,20,22], we observed the five signatures of Weyl fermions described above in quantum transport in $SrRuO_3$. The presence of Weyl fermions in $SrRuO_3$ has also been confirmed by first-principles calculations [16,20,21] and angle-resolved photoemission spectroscopy observations of linear band dispersions [23]. In contrast, the origins of the hump-like Hall effect anomaly are still controversial [24–26]. Various mechanisms have been proposed and discussed, including skyrmion-driven topological Hall effect [17–19] and multichannel anomalous Hall effect (AHE) [25,27–30]. The latter originates from the superposition of AHEs with different signs of hysteresis loops when nonidentical multiple magnetic domains exist. Here, the AHE is an additional contribution to the Hall resistivity due to the localized magnetic moment characteristic of magnetic materials.

It is of crucial importance here to draw a distinction between effects that are specific to $SrRuO_3$ and those of accompanying nature. The skyrmion-driven topological Hall effect is a topological and intrinsic effect, while the

*These authors contributed equally to this work.

†Corresponding author: yuuki.wakabayashi@ntt.com

multichannel AHE is a nontopological and extrinsic one. When the hump-like Hall effect was first observed in $SrRuO_3$, it was attributed to the topological Hall effect arising from the skyrmions generated at the $SrRuO_3/SrIrO_3$ interface [17,18]. On the other hand, the hump-like Hall effect anomaly has been observed when $SrRuO_3$ is composed of magnetically inhomogeneous domains [27–30]. Although Ru deficiencies are considered essential for the inhomogeneity of magnetic domains [27–30], the Ru-deficiency-dependent manifestation of the hump-like Hall effect anomaly has not been systematically investigated because of the difficulty of controlling the amount of Ru deficiency in $SrRuO_3$. Furthermore, for single-layer $SrRuO_3$, this phenomenon is often observed in very thin films (less than ∼6 nm) presumably with interface-driven defects [19,27–35]. Therefore, systematic experiments on the Weyl fermion transport and hump-like Hall effect anomaly in stoichiometric and Ru-deficient films with various thicknesses are required to distinguish topologically trivial or nontrivial transport phenomena.

In this paper, we investigate the magnetotransport properties of epitaxial $SrRuO_3$ and $SrRu_{0.7}O_3$ films grown by machine-learning-assisted molecular beam epitaxy (ML-MBE) [36,37], in which the supply ratios of Sr and Ru during deposition can be controlled at designated values at will. We prepared stoichiometric ($SrRuO_3$) and Ru-deficient ($SrRu_{0.7}O_3$) films with various thicknesses t(= 2–60 nm). We found that a variety of magnetotransport properties that those films show at different temperatures can be classified into three categories, namely, those observed in clean, intermediate, and dirty regimes. For example, Weyl fermion transport is observed only in the clean regime, i.e., in the thick ($\geqslant$10 nm) stoichiometric films at low temperatures; on the other hand, the hump-like Hall effect anomaly is observed only in the dirty regime, i.e., in the thin ($\leqslant$5 nm) Ru-deficient films. We also examined a scaling law between anomalous Hall resistivity and longitudinal resistivity, which is derived from a model incorporating the intrinsic Karplus-Luttinger and extrinsic side-jump mechanisms. While this scaling law can be applied broadly to most $SrRuO_3$ and $SrRu_{0.7}O_3$ films in the clean and intermediate regimes, regardless of stoichiometry, film thickness, and temperature, we found it is not the case for those exhibiting the hump-like Hall effect anomaly (in the dirty regime). We also provide defect- and temperature-dependent transport diagrams for $SrRuO_3$ and $SrRu_{0.7}O_3$ for accessing various electronic states realized in these materials, including the topological one with Weyl fermions and the nontopological one that exhibits the hump-like Hall effect anomaly. The diagrams will serve as a guideline for designing $SrRu_{1-x}O_3$-based spintronic and topological electronic devices.

II. EXPERIMENTS

We grew epitaxial stoichiometric $SrRuO_3$ and Ru-deficient $SrRu_{0.7}O_3$ films with various t(= 2–60 nm) on (001) $SrTiO_3$ substrates in a custom-designed ML-MBE setup equipped with multiple e-beam evaporators [38,39] for Sr and Ru. For the $SrRuO_3$ films, the growth parameters were optimized by Bayesian optimization [36,37], a ML technique for parameter optimization. We precisely controlled the elemental fluxes, even for elements with high melting points, e.g., Ru (2250 °C), by monitoring the flux rates with electron impact emission spectroscopy, and the flux rates are fed back to the power supplies for the e-beam evaporators [39]. The Ru flux rates were set at 0.190 and 0.365 Å/s for the growth of the Ru-deficient and stoichiometric films, respectively, while the Sr flux was kept at 0.98 Å/s. The supplied Ru rates of 0.190 Å/s for Ru-deficient and 0.365 Å/s for stoichiometric films correspond to the Ru/Sr flux ratios of 0.80 (Ru-poor) and 1.54 (Ru-rich), respectively [22,40]. Excessive Ru is known to re-evaporate from the growth surface by forming volatile species such as RuO_4 and RuO_3 under oxidizing atmospheres, and this thermodynamic behavior has been exploited for stoichiometric films [41]. The oxidation during growth was carried out with a mixture of ozone (O_3) and O_2 gas (∼15% O_3 + 85% O_2), which was introduced at a flow rate of ∼2 sccm through an alumina nozzle pointed at the substrate. All $SrRuO_3$ and $SrRu_{0.7}O_3$ films were grown at 772 °C. The chemical compositions of the $SrRuO_3$ and $SrRu_{0.7}O_3$ films with thickness $t = 60$ nm were determined using energy-dispersive x-ray spectroscopy (EDS) [40]. The Ru deficiency in the $SrRu_{0.7}O_3$ film was also confirmed by the chemical shift of the Ru $3p_{3/2}$ x-ray photoelectron spectroscopy (XPS) peak [40]. Further information about the MBE setup [36–39,41], reflection high-energy electron diffraction patterns [22,36,40–42], cross-sectional scanning transmission electron microscopy images [16,22,36,40], surface morphology [20,36], x-ray diffraction patterns [20,22,36,42,43], EDS [40], XPS of stoichiometric $SrRuO_3$ and Ru-deficient $SrRu_{0.7}O_3$ films [40], x-ray absorption [42,44], x-ray magnetic circular dichroism [42,44], and magnetization [16,36,40,42,43] are described elsewhere.

For the measurement of transport properties, we fabricated 200 × 350 μm^2 Hall bar structures by photolithography and Ar ion milling. Before making the Hall bar structure, we deposited Ag electrodes onto $SrRuO_3$ or $SrRu_{0.7}O_3$ surfaces. The longitudinal resistivity $\rho_{xx}(T)$ data in Refs. [22,40] were obtained from the same samples used in this paper but without making the Hall bar. The magnetotransport up to 14 T in the temperature range of 2 to 300 K was measured in a DynaCool physical property measurement system. The magnetic field B was applied in the [001] direction of the $SrTiO_3$ substrate perpendicular to the film plane. The current flow in the specimens is nearly along the in-plane [100] direction of the pseudocubic $SrRuO_3$ and $SrRu_{0.7}O_3$.

III. RESULTS AND DISCUSSION

We performed magnetotransport measurements on the Hall bar devices of the stoichiometric $SrRuO_3$ and Ru-deficient $SrRu_{0.7}O_3$ films with t = 2–60 nm. The temperature (T) dependence of the longitudinal resistivity $\rho_{xx}(T,\ 0\ \mathrm{T})$, residual resistivity ratio (RRR), and the Curie temperature T_C of all the films are summarized in Fig. S1 in the Supplemental Material [45]. In short, we achieved a high RRR > 60 when the film thickness of the stoichiometric film was large ($t = 60$ nm) [16,20,22,36,37,40–43]. The RRR value is a measure of the purity, thus providing information on the degree of impurity (defect) scattering. If RRR > 60, $SrRuO_3$ is regarded as a high-quality material. For $SrRuO_3$ films with t = 5–60 nm and $SrRu_{0.7}O_3$ films with t = 10–60 nm,

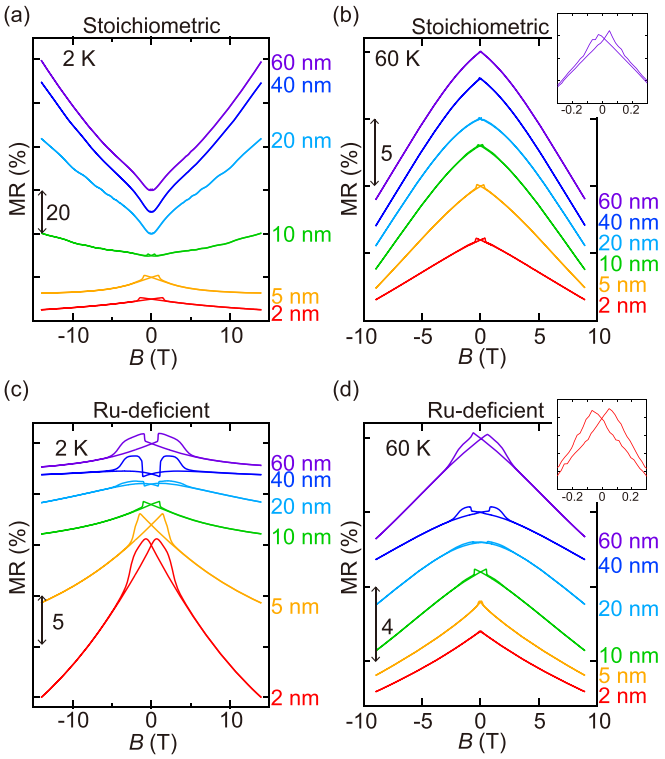

FIG. 1. Thickness t dependence of the MR for [(a) and (b)] the stoichiometric $SrRuO_3$ and [(c) and (d)] the Ru-deficient $SrRu_{0.7}O_3$ films at [(a) and (c)] 2 K and [(b) and (d)] 60 K. B is applied in the out-of-plane [001] direction of the $SrTiO_3$ substrate. The insets are the enlarged anisotropic MR (AMR) of (b) the $SrRuO_3$ film with $t = 60$ nm and (d) the $SrRu_{0.7}O_3$ film with $t = 2$ nm, respectively.

temperature dependencies of $\rho_{xx}(T,\ 0\ \mathrm{T})$ were almost completely preserved after the Hall-bar fabrication, although the absolute values are ∼1.3 times higher, confirming limited fabrication damage, in addition to the high reproducibility of our experiments (Figs. S1(a) and S1(b) in the Supplemental Material [45], and Refs. [22,40]).

A. MR

Figure 1 shows the t dependence of the MR $\{[\rho_{xx}(B) - \rho_{xx}(0\ \mathrm{T})]/\rho_{xx}(0\ \mathrm{T})\}$ of $SrRuO_3$ [Figs. 1(a) and 1(b)] and the $SrRu_{0.7}O_3$ [Figs. 1(c) and 1(d)] films when B was applied in the out-of-plane [001] direction of the $SrTiO_3$ substrate at 2 and 60 K. For stoichiometric $SrRuO_3$ films at 2 K, the sign of MR in the high-B region changed from negative to positive with increasing t [Fig. 1(a)]. The positive linear MR for $t \geqslant 10$ nm at 2 K showed no signature of saturation even up to 14 T, which is commonly seen in Weyl semimetals and is thought to stem from the linear energy dispersion of Weyl nodes [13]. Furthermore, these $SrRuO_3$ films with $t \geqslant 10$ nm showed quantum oscillations in resistivity [i.e., Shubnikov–de Haas (SdH) oscillations], whose frequency (26 T) corresponds to that of the Fermi arc of Weyl fermions with high mobility of 3000 to 10 000 $\mathrm{cm}^2/\mathrm{Vs}$ [16,20,22]. As described in the introduction, these unsaturated linear positive MR and SdH oscillations, which appear simultaneously when $t \geqslant 10$ nm, are incontrovertible facts of Weyl fermion transport in $SrRuO_3$. Accordingly, Weyl fermions also play a vital role in $SrRuO_3$ films processed into the Hall-bar structure. In the case of Ru deficiency, i.e., $SrRu_{0.7}O_3$ films, however, the MR in the high-B region is negative, and the SdH oscillations are not observed for any film even at 2 K, irrespective of the thickness [Fig. 1(c)]. In other words, electronic transport by Weyl fermions may not be dominant, which is consistent with our previous report [40].

At 60 K, all samples show a negative MR due to the suppression of magnetic scattering at high magnetic fields [16], irrespective of thickness and stoichiometry [Figs. 1(b) and 1(d)]. In all films, the anisotropic MR (AMR), which is proportional to the relative angle between the electric current and the magnetization, shows a MR hysteresis where the peak position of the MR corresponds to the coercive field H_C. $SrRu_{0.7}O_3$ films with $t = 20$–60 nm show a rather peculiar AMR shape, and the MR hysteresis appears above ∼1 T [Figs. 1(c) and 1(d)]. This feature has been attributed to the existence of two different magnetic components in the $SrRu_{0.7}O_3$ films [40]. The AMR disappears above T_C, reflecting the paramagnetic states (Figs. S2(c) and S2(d) in the Supplemental Material [45]).

B. The Hall effect

Figures 2(a) and 2(b) [2(c) and 2(d)] show the B dependence of the Hall resistivity $\rho_{xy}(B)$ for the stoichiometric $SrRuO_3$ [Ru-deficient $SrRu_{0.7}O_3$] films at 2 and 60 K, well below the T_C values of each film (Fig. S1(f) in the Supplemental Material [45]). The $\rho_{xy}(B)$ curves are sectioned into three categories based on their qualitative characteristics: (1) the clean regime where $SrRuO_3$ films with $t \geqslant 10$ nm (RRR > ∼20) show the Weyl fermion transport at low temperatures below ∼20 K, (2) the intermediate regime where the Weyl fermion transport is suppressed and the topologically trivial conduction electrons in the ferromagnetic metal govern the transport phenomenon, and (3) the dirty regime where the hump-like Hall effect anomaly emerges in the Ru-deficient $SrRu_{0.7}O_3$ films with $t \leqslant 5$ nm (RRR < 3.5).

1. Clean regime: $SrRuO_3$ with $t = 10$–60 nm measured at 2 K

The $\rho_{xy}(B)$ curves for the stoichiometric $SrRuO_3$ films with $t = 10$–60 nm at 2 K vary monotonically with negative (positive) slopes at low (high)-B ranges. This nonlinear behavior is reminiscent of semimetals with multiple carrier types [Fig. 2(a)]. In ultrahigh-quality $SrRuO_3$ films with $t = 10$–60 nm, Weyl fermion transport dominates at 2 K, and accordingly, the observed $\rho_{xy}(B)$ behavior is assumed to be determined by Weyl fermions in the Weyl semimetal state. This is further supported by the SdH oscillations superimposed to the $\rho_{xy}(B)$ curves [see inset of Fig. 2(a) as an example], which can be attributed to two-dimensional Weyl fermion transport from surface Fermi arcs [20]. This in turn indicates that the B dependence of the Hall resistivity characteristic of semimetals may be utilized as another signature of the Weyl fermion transport in $SrRuO_3$.

Although Weyl fermions in solids follow a linear dispersion relation while there are several Weyl points around the Fermi energy (E_F) within a single Brillouin zone of $SrRuO_3$ [16], a discussion using a two-carrier model assuming

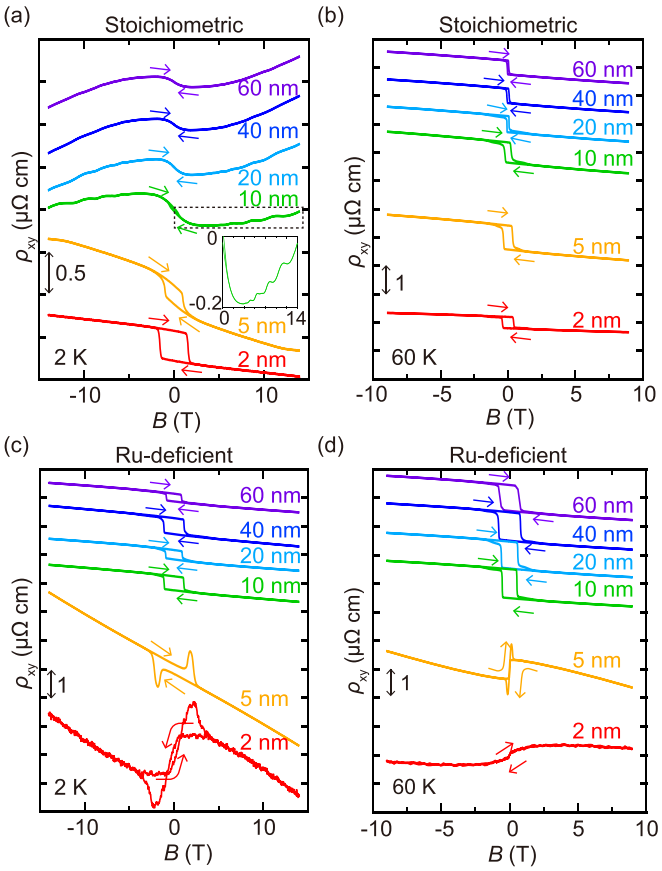

FIG. 2. Thickness t dependence of the Hall resistivity ρ_{xy} for [(a) and (b)] the stoichiometric $SrRuO_3$ and [(c) and (d)] the Ru-deficient $SrRu_{0.7}O_3$ films at [(a) and (c)] 2 K and [(b) and (d)] 60 K. B is applied in the out-of-plane [001] direction of the $SrTiO_3$ substrate. The arrows indicate the sweep direction of B.

two (one convex-upward and the other downward) quadratic dispersions would provide some clues to the interpretation of the $\rho_{xy}(B)$ data [46]. According to the two-carrier model, the sign and the slope of $\rho_{xy}(B)$ in the high-B limit reflect the major carrier type and the difference between the major-carrier and minor-carrier densities, respectively. The positive sign in the high-B range is indicative for hole-like Weyl fermions. The negative slope in the low-B range may reflect on the fact that μ_e is higher than μ_h because p is higher than n [46]. Here, p, n, μ_h, and μ_e are the hole carrier density, electron carrier density, hole mobility, and electron mobility, respectively. While topologically trivial conduction electrons in the metallic state of $SrRuO_3$ may also contribute to the observed Hall resistivity, the striking contrast between the data for the stoichiometric $SrRuO_3$ films with 10–60 nm measured at 2 K and those measured at 60 K [Figs. 2(a) and 2(b)]—e.g., the slope is positive for the former and negative for the latter in the high-B ranges—suggests that the Weyl fermion transport prevails at 2 K. Although the nonlinear-B behavior of $\rho_{xy}(B)$ together with the oversimplified two-carrier model renders an exact estimation of the carrier densities inaccurate, the slope of $\rho_{xy}(B)$ in the high-B range gives a carrier density in the range of 10^{22} cm^{-3}. This is much larger than that estimated from the SdH oscillations ($\sim 10^{17}$–10^{18} cm^{-3}) [16], where only charge carriers that complete cyclotron orbits during their lifetimes are counted. While the monotonic variation of $\rho_{xx}(T,\ 0\ \mathrm{T})$ with decreasing T for $T \leqslant 60$ K (Fig. S1(a) in the Supplemental Material [45]) implies no dramatic change of the majority charge carriers from the topologically trivial conduction electrons to the Weyl fermions but rather a crossover, Weyl fermion transport is prominent in measurements under magnetic fields such as Hall effect, SdH oscillations, and MR at low temperatures.

2. *Intermediate regime: $SrRuO_3$ with $t = 2$–5 nm measured at 2 K, $SrRuO_3$ with $t = 2$–60 nm measured at 60 K, and $SrRu_{0.7}O_3$ with $t = 10$–60 nm measured at 2 or 60 K*

The transport properties in this category are subject to substantial scattering due to defects and/or phonons. The defect-induced scattering is characterized by low RRR, and the defects are interface and/or Ru-deficiency driven. The scattering events take place too frequently, and Weyl fermion transport and SdH oscillations are marginalized (Fig. 2) [40]. Thus, the observed Hall effect can be attributed to the topologically trivial conduction electrons in the metallic $SrRuO_3$ or $SrRu_{0.7}O_3$. Note that the $SrRuO_3$ film with $t = 5$ nm at 2 K may have $\rho_{xy}(B)$ characteristics between clean and intermediate regimes. In the intermediate regime, the magnetization hysteresis curve characteristic of the AHE is clearly observed, and it dominates Hall resistivity at near-zero magnetic fields ($\rho_{xy,0\ \mathrm{T}}$). This is quite in contrast to the clean regime, where the AHE components are negligibly small due to the small ρ_{xx} values; $\rho_{xy,0\ \mathrm{T}}$ is proportional to ρ_{xx}^2 at low enough temperatures. Above T_C (at 180 K), $\rho_{xy,0\ \mathrm{T}}$ of all the films becomes zero, reflecting the paramagnetic states (Fig. S2(a) in the Supplemental Material [45]). The temperature dependence of the AHE will be discussed in detail later (Sec. III C) regarding the scaling law between ρ_{xy} and ρ_{xx}.

The ordinary Hall effect [linear $\rho_{xy}(B)$] at high B in metals depends on the energy band dispersion [e.g., $dE(\mathbf{k})/d\mathbf{k}$] near E_F and on $\mathbf{k}$-dependent (anisotropic) relaxation times [$\tau(\mathbf{k})$] [47]. Hence, the interpretation of the data is not straightforward. More so, $SrRuO_3$ has spin-polarized electron bands for $T < T_C$, and its Fermi surface consist of at least six sheets, including open orbits [48]. Accordingly, the Hall coefficient is not related to the carrier density in any simple manner [47]. Nonetheless, the identical $\rho_{xy}(B)$ slopes in the data except for very thin films (2–5 nm) indicate that the electronic structure, $\tau(\mathbf{k})$, and the carrier density are comparable among the films assigned to the intermediate regime. Supposing that $\tau(\mathbf{k})$ on one of the Fermi sheets (closed and isotropic) is significantly longer than the others and governs the Hall effect, the slope of $\rho_{xy}(B)$ would provide an effective carrier (electron) density of $\sim 2 \times 10^{22}$ cm^{-3} [46]; the corresponding charge carrier mobility at 60 K would be 7–9 cm^2/Vs and 3–4 cm^2/Vs for $SrRuO_3$ and $SrRu_{0.7}O_3$ with $t = 10$–60 nm, respectively (Fig. S3 in the Supplemental Material [45]). Unexpectedly, the slopes of $\rho_{xy}(B)$ in the high-B range for stoichiometric and Ru-deficient films ($t = 10$–60 nm) at 60 K are identical; nevertheless the band filling factor should be different between $SrRuO_3$ and $SrRu_{0.7}O_3$ within a rigid band model. This might be explained by assuming a common Fermi surface that mostly governs the Hall effect whose geometry

is unchanged by Ru vacancies, while only filling factors of bands with substantially shorter $\tau(\mathbf{k})$ at E_F vary with the Ru composition.

3. Dirty regime: $SrRu_{0.7}O_3$ with $t = 2$–5 nm measured at 2 or 60 K

The AHEs with hump structures are prominent in the Ru-deficient films with $t = 2$ and 5 nm at 2 K [Fig. 2(c)]. At 60 K, this hump-like Hall effect anomaly for $t = 2$ nm disappears, while persisting for $t = 5$ nm [Fig. 2(d)]. Previous studies have suggested that these hump-like Hall effect anomalies in $SrRuO_3$ are associated to the topological Hall effect [17–19] and the multichannel AHEs from the superposition of two different AHE components [27–30]. In our films, the humps are observed only for Ru-deficient $SrRu_{0.7}O_3$ thin films, indicating that Ru deficiencies play an important role in the appearance of the humps, i.e., it does not have an intrinsic or topological origin. Instead, it is known that this material shows different signs of the AHE depending on T [49]. The net AHE can be accompanied by a hump structure if the temperature at which its sign changes differs among some multiple magnetic domains [27,30]. The absence of the humps in the $SrRuO_3$ films with $t = 2$–60 nm and the $SrRu_{0.7}O_3$ films with $t = 10$–60 nm indicates that these films have no spatial variation of the temperature at which the sign of AHE changes.

C. Further analysis of AHE: Quest for the origin

Various theoretical models have been proposed for the origin of the AHE in magnetic materials, including the Karplus-Luttinger mechanism [50,51] as an intrinsic origin and the side-jump [52,53] and skew-scattering mechanisms [54,55] as extrinsic origins. The intrinsic Karplus-Luttinger term originates from the geometry of the band structure [56]. The Karplus-Luttinger term can contribute to the AHE for both topologically trivial conduction electrons and Weyl fermions. To examine the origin of the AHE in our $SrRuO_3$ and $SrRu_{0.7}O_3$ films, we measured the temperature dependence of the AHE. Figures 3(a) and 3(b) show the T dependence of the remanent Hall resistivity ρ_{xy} at 0 T for stoichiometric $SrRuO_3$ and Ru-deficient $SrRu_{0.7}O_3$ films. Here, $\rho_{xy,0\,T}$ is the ρ_{xy} value at 0 T after sweeping from high B (9 or 14 T) to 0 T (Fig. S4 in the Supplemental Material [45]). The position of kinks in $\rho_{xx}(T)$ curves (Fig. S1 in the Supplemental Material [45]) are used to determine T_C. Irrespective of stoichiometry and thickness, $\rho_{xy,0\,T}$ becomes zero above T_C (Figs. S2(a) and S2(b) in the Supplemental Material [45]), reflecting the paramagnetic states [56]. Except for the $SrRu_{0.7}O_3$ films with $t = 2$ and 5 nm, the $\rho_{xy,0\,T}$ curves show positive peaks around T_C, and then the values change from positive to negative with decreasing T. For even lower temperatures, $\rho_{xy,0\,T}$ values increase. This trend has been attributed to a combination of the intrinsic Karplus-Luttinger and extrinsic side-jump mechanisms [49,51–53]. For the scaling analysis of $\rho_{xy,0\,T}$ to ρ_{xx}, we defined $\rho'_{xy,0\,T}$ and ρ'_{xx} as $\rho_{xy,0\,T}$ normalized by its maximum absolute value and ρ_{xx} normalized by its value when $\rho_{xy,0\,T}$ changes its sign, respectively. Figure 3(c) shows the $\rho'_{xy,0\,T}$ vs ρ'_{xx} curves for the $SrRuO_3$ films with $t = 2$–60 nm and the $SrRu_{0.7}O_3$ films with $t = 10$–60 nm. The $\rho'_{xy,0\,T}$ vs ρ'_{xx} curves

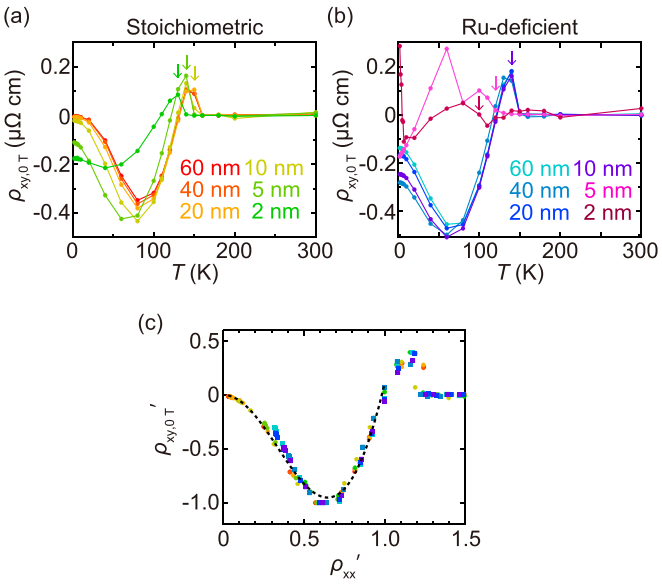

FIG. 3. Remanent Hall resistivity $\rho_{xy,0\,T}$ vs temperature T curves for (a) the stoichiometric $SrRuO_3$ and (b) the Ru-deficient $SrRu_{0.7}O_3$ films with $t = 2$–60 nm. (c) Normalized remanent Hall resistivity $\rho'_{xy,0\,T}$ vs normalized longitudinal resistivity ρ'_{xx} curves for the stoichiometric $SrRuO_3$ and Ru-deficient $SrRu_{0.7}O_3$ films, excluding the Ru-deficient $SrRu_{0.7}O_3$ films with $t = 2$ and 5 nm. The dashed line is the fitting of a scaling law by Eq. (1).

for the Ru-deficient $SrRu_{0.7}O_3$ films with $t = 2$ and 5 nm are also shown in Fig. S5 in the Supplemental Material [45]. Regardless of stoichiometry, thickness, and temperature at which $|\rho_{xy,0\,T}|$ becomes maximum, all $\rho'_{xy,0\,T}$-ρ'_{xx} curves coincide, indicating that a universal scaling law exists independent of scattering frequency and sources, i.e., Ru-deficiency- or interface-driven defects, or phonons. However, Ru-deficient $SrRu_{0.7}O_3$ films with $t = 2$ and 5 nm that show the hump-like Hall effect anomaly [Figs. 2(c) and 2(d)] deviate from this trend (Fig. S5 in the Supplemental Material [45]). This indicates that the hump-like Hall effect anomaly cannot be explained by the Karplus-Luttinger or side-jump mechanisms. More importantly, this anomaly is not inherent to the material system of $SrRu_{1-x}O_3$. We fit $\rho'_{xy,0\,T}$-ρ'_{xx} curves using the scaling law expressed as follows [49]:

$$\rho'_{xy,0\,T} = \frac{a_1}{\Delta^2 + a_2(\rho'_{xx})^2}(\rho'_{xx})^2 + a_3(\rho'_{xx})^2, \qquad (1)$$

where a_1–a_3 and Δ are fitting parameters, which are related to the band structure of $SrRuO_3$ [49]. The first term describes the contribution from the Karplus-Luttinger mechanism, in which scattering in the stoichiometric $SrRuO_3$ and Ru-deficient $SrRu_{0.7}O_3$ films are considered as the imaginary part of the self-energy of Kubo's formula [56], and the second term that from the side-jump scattering. As shown in Fig. 3(c), all our experimental data are well fitted by a single set of parameters: $a_1 = -2.3 \times 10^{16}$, $a_2 = 1.3 \times 10^{15}$, $a_3 = 7.4$, and $\Delta = 4.2 \times 10^7$. This universal scaling of the AHE in the $SrRuO_3$ films with $t = 2$–60 nm and the $SrRu_{0.7}O_3$ films with $t = 10$–60 nm (in the clean and intermediate regimes) supports a common origin from combined Karplus-Luttinger and side-jump mechanisms. The universal scaling also indi-

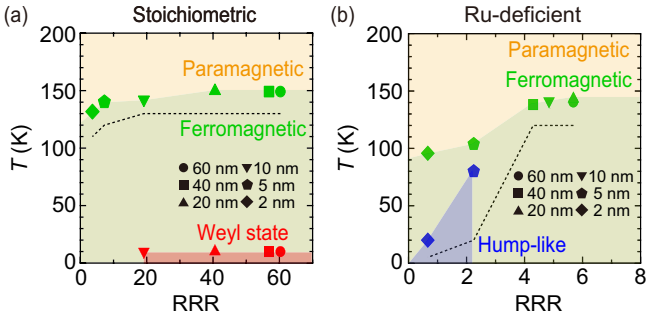

FIG. 4. RRR and temperature dependence of the transport phenomena in (a) the stoichiometric $SrRuO_3$ and (b) Ru-deficient $SrRu_{0.7}O_3$ films. Here, red, blue, and green plots are the highest temperature where the Weyl fermion transport appears, the highest temperature where the hump-like Hall effect anomaly appears, and T_C. Shaded red, green, and blue areas roughly correspond to the clean, intermediate, and dirty regimes, respectively, defined based on the results of the Hall effect experiments (see text). The dashed lines indicate the temperatures where $\rho_{xy,0\,\mathrm{T}}$ changes its sign.

cates that the remanent Hall resistivity $\rho_{xy,0\,\mathrm{T}}$ is determined by the scattering rate, regardless of the relative contributions of the different scattering processes. From Fig. 3(c), in the region of $\rho_{xx}^{'} < 1.0$ ($\rho_{xy,0\,\mathrm{T}}^{'} < 0$), the contribution from the Karplus-Luttinger mechanism is dominant. On the other hand, in the region of $\rho_{xx}^{'} > 1.0$ ($\rho_{xy,0\,\mathrm{T}}^{'} > 0$), the contribution from the side-jump scattering is dominant.

D. RRR and temperature-dependent transport diagram

Finally, we summarize the magnetotransoprt results on RRR-temperature diagrams (Fig. 4) and depict the regions where the Weyl fermion transport or the hump-like Hall effect anomaly emerges. Again, the RRR is known to be an important measure of the crystal purity, i.e., defect density, which was controlled by Ru deficiencies and/or interface defects. The transport phase diagram for stoichiometric $SrRuO_3$ [Fig. 4(a)] is consistent with what we have shown before [16] except for the very low RRR ($\leqslant 10$) regime. Note that, the previous transport phase diagram in Ref. [16] was prepared using the data obtained during the growth condition optimization procedure for 63-nm-thick $SrRuO_3$ films. The different RRR values may originate from Ru and/or O vacancies and orthorhombic domains. First, the Weyl fermion transport appears only if RRR is high and T is low [Fig. 4(a)]. This observation is physically reasonable, as Weyl fermion transport is vulnerable to scattering. Second, the Weyl fermion transport disappears, and the topologically trivial conduction electrons in the ferromagnetic metal govern the transport phenomenon in the intermediate regime. Finally, the hump-like Hall effect anomaly emerges only if RRR is low [Fig. 4(b)]. More specifically, the hump-like Hall effect anomaly is observed in Ru-deficient $SrRu_{0.7}O_3$ films with $t \leqslant 5$ nm (RRR $< \sim$2.2) but not in the 2-nm-thick stoichiometric $SrRuO_3$ film (RRR ~ 3.6). This indicates that the hump-like Hall effect anomaly is caused by the coexistence of Ru deficiencies and interface-driven defects. In fact, this anomaly has been reported often for very thin films (< 6 nm) [19,27–35]. A considerable number of defects is a prerequisite for the emergence of the hump-like Hall effect anomaly, and it does not have an intrinsic or topological origin.

IV. SUMMARY

In summary, we have investigated the magnetotransport properties of epitaxial stoichiometric $SrRuO_3$ and Ru-deficient $SrRu_{0.7}O_3$ films with various thicknesses ($t =$ 2–60 nm). We found that the emergence of the Weyl fermion and hump-like Hall effect anomaly is governed by the degree of scattering. With respect to scattering, we categorized magnetotransport properties into clean, intermediate, and dirty regimes.

(1) In the clean regime, $SrRuO_3$ films with $t \geqslant 10$ nm (RRR $> \sim$20) show the Weyl fermion transport behavior (linear positive MR, SdH oscillations, and Hall effect characteristic of semimetals) at low temperatures below $\sim$20 K.

(2) In the intermediate regime, the Weyl fermion transport disappears, and the topologically trivial conduction electrons in the ferromagnetic metal govern the transport phenomenon; the ordinary Hall effect is observed and accompanied by the AHE. The ordinary Hall effect suggests that the electronic structure and Fermi surface geometry are common among the $SrRuO_3$ and $SrRu_{0.7}O_3$ films classified in this category. We analyzed the correlation between the anomalous Hall resistivity [$\rho_{xy,0\,\mathrm{T}}(T)$] and the longitudinal resistivity [$\rho_{xx}(T)$] using a combination of the intrinsic Karplus-Luttinger and the extrinsic side-jump mechanisms. This results in a universal scaling law for the clean and intermediate regimes, independent of scattering frequency and sources.

(3) In the dirty regime, the hump-like Hall effect anomaly emerges in the Ru-deficient $SrRu_{0.7}O_3$ films with $t \leqslant 5$ nm (RRR < 2.2). The scaling law between $\rho_{xy,0\,\mathrm{T}}$ and ρ_{xx} established for the clean and intermediate regimes does not hold in the dirty regime, indicating that the hump-like Hall effect cannot be explained by the adopted model and is not inherent to $Sr\,Ru_{1-x}O_3$.

The defect- and temperature-dependent transport diagrams of $SrRuO_3$ and $SrRu_{0.7}O_3$ may serve as a guideline for the development of $Sr\,Ru_{1-x}O_3$-based spintronic and topological electronic devices that exploit various electronic and magnetic states.

The data that support the findings of this paper are available from the corresponding author upon reasonable request.

ACKNOWLEDGMENTS

S.K.T. acknowledges the support from the Japan Society for the Promotion of Science Fellowships for Young Scientists.

Y.K.W. conceived the idea, designed the experiments, and directed and supervised the project. Y.K.W. and Y.K. grew the samples. S.K.T., Y.K.W., and H.I. fabricated the Hall bar structures. S.K.T. and Y.K.W. carried out the magnetotransport measurements. S.K.T. and Y.K.W. analyzed and interpreted the data. S.K.T. and Y.K.W. cowrote the paper with input from all authors.

The authors declare no competing interests.

[1] Q. L. He, T. L. Hughes, N. P. Armitage, Y. Tokura, and K. L. Wang, Topological spintronics and magnetoelectronics, Nat. Mater. **21**, 15 (2022).

[2] R. Tomasello, E. Martinez, R. Zivieri, L. Torres, M. Carpentieri, and G. Finocchio, A strategy for the design of skyrmion racetrack memories, Sci. Rep. **4**, 6784 (2014).

[3] X. Zhang, G. P. Zhao, H. Fangohr, J. P. Liu, W. X. Xia, and F. J. Morvan, Skyrmion-skyrmion and skyrmion-edge repulsions in skyrmion-based racetrack memory, Sci. Rep. **5**, 7643 (2015).

[4] N. Nagaosa and Y. Tokura, Topological properties and dynamics of magnetic skyrmions, Nat. Nanotech. **8**, 899 (2013).

[5] C. H. Lee, S. Imhof, C. Berger, F. Bayer, J. Brehm, L. W. Molenkamp, T. Kiessling, and R. Thomale, Topoelectrical Circuits, Commun. Phys. **1**, 39 (2018).

[6] S. M. Rafi-Ul-Islam, Z. B. Siu, and M. B. A. Jalil, Topoelectrical circuit realization of a Weyl semimetal heterojunction, Commun. Phys. **3**, 72 (2020).

[7] N. Morali, R. Batabyal, P. K. Nag, E. Liu, Q. Xu, Y. Sun, B. Yan, C. Felser, N. Avraham, and H. Beidenkopf, Fermi-arc diversity on surface terminations of the magnetic Weyl semimetal $Co_3Sn_2S_2$, Science **365**, 1286 (2019).

[8] D. F. Liu, A. J. Liang, E. K. Liu, Q. N. Xu, Y. W. Li, C. Chen, D. Pei, W. J. Shi, S. K. Mo, P. Dudin *et al.*, Magnetic Weyl semimetal phase in a kagomé crystal, Science **365**, 1282 (2019).

[9] S. -Y. Xu, I. Belopolski, N. Alidoust, M. Neupane, G. Bian, C. Zhang, R. Sankar, G. Chang, Z. Yuan, C.-C. Lee *et al.*, Discovery of a Weyl fermion semimetal and topological Fermi arcs, Science **349**, 613 (2015).

[10] S.-M. Huang, S.-Y. Xu, I. Belopolski, C.-C. Lee, G. Chang, B. Wang, N. Alidoust, G. Bian, M. Neupane, C. Zhang *et al.*, A Weyl Fermion semimetal with surface Fermi arcs in the transition metal monopnictide TaAs class, Nat. Commun. **6**, 7373 (2015).

[11] B. Q. Lv, H. M. Weng, B. B. Fu, X. P. Wang, H. Miao, J. Ma, P. Richard, X. C. Huang, L. X. Zhao, G. F. Chen *et al.*, Experimental Discovery of Weyl Semimetal TaAs, Phys. Rev. X **5**, 031013 (2015).

[12] I. Belopolski, K. Manna, D. S. Sanchez, G. Chang, B. Ernst, J. Yin, S. S. Zhang, T. Cochran, N. Shumiya, H. Zheng *et al.*, Discovery of topological Weyl fermion lines and drumhead surface states in a room temperature magnet, Science **365**, 1278 (2019).

[13] X. Huang, L. Zhao, Y. Long, P. Wang, D. Chen, Z. Yang, H. Liang, M. Xue, H. Weng, Z. Fang *et al.*, Observation of the Chiral-Anomaly-Induced Negative Magnetoresistance in 3D Weyl Semimetal TaAs, Phys. Rev. X **5**, 031023 (2015).

[14] A. Neubauer, C. Pfleiderer, B. Binz, A. Rosch, R. Ritz, P. G. Niklowitz, and P. Böni, Topological Hall Effect in the *A* Phase of MnSi, Phys. Rev. Lett. **102**, 186602 (2009).

[15] Y. Chen, D. L. Bergman, and A. A. Burkov, Weyl fermions and the anomalous Hall effect in metallic ferromagnets, Phys. Rev. B **88**, 125110 (2013).

[16] K. Takiguchi, Y. K. Wakabayashi, H. Irie, Y. Krockenberger, T. Otsuka, H. Sawada, S. A. Nikolaev, H. Das, M. Tanaka, Y. Taniyasu *et al.*, Quantum transport evidence of Weyl fermions in an epitaxial ferromagnetic oxide, Nat. Commun. **11**, 4969 (2020).

[17] J. Matsuno, N. Ogawa, K. Yasuda, F. Kagawa, W. Koshibae, Y. Tokura N.Nagaosa, and M. Kawasaki, Interface-driven topological Hall effect in $SrRuO_3$-$SrIrO_3$ bilayer, Sci. Adv. **2**, e1600304 (2016).

[18] Y. Ohuchi, J. Matsuno, N. Ogawa, Y. Kozuka, M. Uchida,Y. Tokura, and M. Kawasaki, Electric-field control of anomalous and topological Hall effects in oxide bilayer thin films, Nat. Commun. **9**, 213 (2018).

[19] Q. Qin, L. Liu, W. Lin, X. Shu, Q. Xie, Z. Lim, C. Li, S. He, G. M. Chow, and J. Chen, Emergence of topological Hall effect in a $SrRuO_3$ single layer, Adv. Mater. **31**, 1807008 (2019).

[20] S. Kaneta-Takada, Y. K. Wakabayashi, Y. Krockenberger, T. Nomura, Y. Kohama, S. A. Nikolaev, H. Das, H. Irie, K. Takiguchi, S. Ohya *et al.*, High-mobility two-dimensional carriers from surface Fermi arcs in magnetic Weyl semimetal films, npj Quantum Mater. **7**, 102 (2022).

[21] U. Kar, A. K. Singh, Y.-T. Hsu, C.-Y. Lin, B. Das, C.-T. Cheng, M. Berben, S. Yang, C.-Y. Lin, C.-H. Hsu *et al.*, The thickness dependence of quantum oscillations in ferromagnetic Weyl metal $SrRuO_3$, npj Quantum Mater. **8**, 8 (2023).

[22] S. Kaneta-Takada, Y. K. Wakabayashi, Y. Krockenberger, S. Ohya, M. Tanaka, Y. Taniyasu, and H. Yamamoto, Thickness-dependent quantum transport of Weyl fermions in ultra-high-quality $SrRuO_3$ films, Appl. Phys. Lett. **118**, 092408 (2021).

[23] W. Lin, L. Liu, Q. Liu, L. Li, X. Shu, C. Li, Q. Xie, P. Jiang, X. Zheng, R. Guo *et al.*, Electric field control of the magnetic Weyl fermion in an epitaxial $SrRuO_3$ (111) thin film, Adv. Mater. **33**, 2101316 (2021).

[24] G. Kimbell, C. Kim, W. Wu, M. Cuoco, and J. W. A. Robinson, Challenges in identifying chiral spin textures via the topological Hall effect, Commun. Mater. **3**, 19 (2022).

[25] M. Cuoco and A. D. Bernardo, Materials challenges for $SrRuO_3$: From conventional to quantum electronics, APL Mater. **10**, 090902 (2022).

[26] Y. Gu, Q. Wang, W. Hu, W. Liu, Z. Zhang, F. Pan, and C. Song, An overview of $SrRuO_3$-based heterostructures for spintronic and topological phenomena, J. Phys. D: Appl. Phys. **55**, 233001 (2022).

[27] D. Kan, T. Moriyama, K. Kobayashi, and Y. Shimakawa, Alternative to the topological interpretation of the transverse resistivity anomalies in $SrRuO_3$, Phys. Rev. B **98**, 180408(R) (2018).

[28] D. Kan and Y. Shimakawa, Defect-induced anomalous transverse resistivity in an itinerant ferromagnetic oxide, Phys. Status Solidi B **255**, 1800175 (2018).

[29] G. Kimbell, P. M. Sass, B. Woltjes, E. K. Ko, T. W. Noh, W. Wu, and J. W. A. Robinson, Two-channel anomalous Hall effect in $SrRuO_3$, Phys. Rev. Mater. **4**, 054414 (2020).

[30] G. Kim, K. Son, Y. E. Suyolcu, L. Miao, N. J. Schreiber, H. P. Nair, D. Putzky, M. Minola, G. Christiani, P. A. van Aken *et al.*, Inhomogeneous ferromagnetism mimics signatures of the topological Hall effect in $SrRuO_3$ films, Phys. Rev. Mater. **4**, 104410 (2020).

[31] D. Kan, T. Moriyama, and Y. Shimakawa, Field-sweep-rate and time dependence of transverse resistivity anomalies in ultrathin $SrRuO_3$ films, Phys. Rev. B **101**, 014448 (2020).

[32] B. Sohn, B. Kim, J. W. Choi, S. H. Chang, J. H. Han, and C. Kim, Hump-like structure in Hall signal from ultra-thin $SrRuO_3$ films without inhomogeneous anomalous Hall effect, Curr. Appl. Phys. **20**, 186 (2020).

[33] L. Wysocki, L. Yang, F. Gunkel, R. Dittmann, P. H. M. van Loosdrecht, and I. Lindfors-Vrejoiu, Validity of

magnetotransport detection of skyrmions in epitaxial $SrRuO_3$ heterostructures, Phys. Rev. Mater. **4**, 054402 (2020).

[34] L. Yang, L. Wysocki, J. Schöpf, L. Jin, A. Kovács, F. Gunkel, R. Dittmann, P. H. M. van Loosdrecht, and I. Lindfors-Vrejoiu, Origin of the hump anomalies in the Hall resistance loops of ultrathin $SrRuO_3/SrIrO_3$ multilayers, Phys. Rev. Mater. **5**, 014403 (2021).

[35] M. Zhu, Z. Cui, W. Li, Z. Shan, J. Wang, H. Huang, Z. Fu, and Y. Lu, Anomalous Hall effect in spatially inhomogeneous $SrRuO_3$ films, AIP Adv. **11**, 125027 (2021).

[36] Y. K. Wakabayashi, T. Otsuka, Y. Krockenberger, H. Sawada, Y. Taniyasu, and H. Yamamoto, Machine-learning-assisted thin-film growth: Bayesian optimization in molecular beam epitaxy of $SrRuO_3$ thin films, APL Mater. **7**, 101114 (2019).

[37] Y. K. Wakabayashi, T. Otsuka, Y. Krockenberger, H. Sawada, Y. Taniyasu, and H. Yamamoto, Bayesian optimization with experimental failure for high-throughput materials growth, npj Comput. Mater. **8**, 180 (2022).

[38] H. Yamamoto, Y. Krockenberger, Y. Taniayasu, and Y. K. Wakabayashi, Electron-beam-evaporation-based multi-source oxide MBE as a synthesis method for high-quality and novel magnetic materials—Beyond 3*d* transition metal compounds, J. Cryst. Growth **593**, 126778 (2022).

[39] H. Yamamoto, Y. Krockenberger, and M. Naito, Multi-source MBE with high-precision rate control system as a synthesis method *sui generis* for multi-cation metal oxides, J. Cryst. Growth **378**, 184 (2013).

[40] Y. K. Wakabayashi, S. Kaneta-Takada, Y. Krockenberger, K. Takiguchi, S. Ohya, M. Tanaka, Y. Taniyasu, and H. Yamamoto, Structural and transport properties of highly Ru-deficient $SrRu_{0.7}O_3$ thin films prepared by molecular beam epitaxy: Comparison with stoichiometric $SrRuO_3$, AIP Adv. **11**, 035226 (2021).

[41] Y. K. Wakabayashi, Y. Krockenberger, T. Otsuka, H. Sawada, Y. Taniyasu, and H. Yamamoto, Intrinsic physics in magnetic Weyl semimetal $SrRuO_3$ films addressed by machine-learning-assisted molecular beam epitaxy, Jpn. J. Appl. Phys. **62**, SA0801 (2022).

[42] Y. K. Wakabayashi, M. Kobayashi, Y. Takeda, K. Takiguchi, H. Irie, S.-i. Fujimori, T. Takeda, R. Okano, Y. Krockenberger, Y. Taniyasu *et al.*, Single-domain perpendicular magnetization induced by the coherent O 2*p*-Ru 4*d* hybridized state in an ultra-high-quality $SrRuO_3$ film, Phys. Rev. Mater. **5**, 124403 (2021).

[43] Y. K. Wakabayashi, S. Kaneta-Takada, Y. Krockenberger, Y. Taniyasu, and H. Yamamoto, Wide-range epitaxial strain control of electrical and magnetic properties in high-quality $SrRuO_3$ films, ACS Appl. Electron. Mater. **3**, 2712 (2021).

[44] Y. K. Wakabayashi, M. Kobayashi, Y. Takeda, M. Kitamura, T. Takeda, R. Okano, Y. Krockenberger, Y. Taniyasu, and H. Yamamoto, Isotropic orbital magnetic moments in magnetically anisotropic $SrRuO_3$ films, Phys. Rev. Mater. **6**, 094402 (2022).

[45] See Supplemental Material at http://link.aps.org/supplemental/10.1103/PhysRevMaterials.7.054406 for the transport characteristics of stoichiometric $SrRuO_3$ and Ru-deficient $SrRu_{0.7}O_3$ films, magnetotransport of the stoichiometric $SrRuO_3$ and Ru-deficient $SrRu_{0.7}O_3$ films above TC, thickness dependence of the carrier density and mobility for $SrRuO_3$ and Ru-deficient $SrRu_{0.7}O_3$ films, the definition of, and the vs curves for all $SrRuO_3$ and Ru-deficient $SrRu_{0.7}O_3$ films.

[46] R. A. Smith, *Semiconductors* (Cambridge University Press, Cambridge, 1978).

[47] C. M. Hurd, *The Hall Effect in Metals and Alloys* (Plenum Press, New York, 1972).

[48] G. Santi and T. Jarlborg, Calculation of the electronic structure and the magnetic properties of $SrRuO_3$ and $CaRuO_3$, J. Phys. Cond. Mat. **9**, 9563 (1997).

[49] N. Haham, Y. Shperber, M. Schultz, N. Naftalis, E. Shimshoni, J. W. Reiner, and L. Klein, Scaling of the anomalous Hall effect in $SrRuO_3$, Phys. Rev. B **84**, 174439 (2011).

[50] H. Kontani, T. Tanaka, and K. Yamada, Intrinsic anomalous Hall effect in ferromagnetic metals studied by the multi-*d*-orbital tight binding model, Phys. Rev. B **75**, 184416 (2007).

[51] R. Karplus and J. M. Luttinger, Hall effect in ferromagnetics, Phys. Rev. **95**, 1154 (1954).

[52] L. Berger, Side-jump mechanism for the Hall effect of ferromagnets, Phys. Rev. B **2**, 4559 (1970).

[53] L. Berger, Application of the side-jump model to the Hall effect and Nernst effect in ferromagnets, Phys. Rev. B **5**, 1862 (1972).

[54] J. Smit, The spontaneous Hall effect in ferromagnetics I, Physica **21**, 877 (1955).

[55] J. Smit, The spontaneous Hall effect in ferromagnetics II, Physica **24**, 39 (1958).

[56] N. Haham, J. W. Reiner, and L. Klein, Scaling of the paramagnetic anomalous Hall effect in $SrRuO_3$, Phys. Rev. B **86**, 144414 (2012).